Title

Tau Assembly: The Dominant Role of PHF6 (VQIVYK) in Microtubule Binding Region Repeat R3

Journal

The Journal of Physical Chemistry B, 119(13)

ISSN

1520-6106

Authors

Ganguly, Pritam
D., Thanh
Larini, Luca
et al.

Publication Date

2015-04-02

DOI

10.1021/acs.jpcb.5b00175

Peer reviewed

HHS Public Access

Author manuscript

J Phys Chem B. Author manuscript; available in PMC 2015 May 12.

Published in final edited form as:

J Phys Chem B. 2015 April 2; 119(13): 4582–4593. doi:10.1021/acs.jpcb.5b00175.

Tau Assembly: The Dominant Role of PHF6 (VQIVYK) in Microtubule Binding Region Repeat R3

Pritam Ganguly[†], **Thanh D. Do**[†], **Luca Larini**[†,§], **Nichole E. LaPointe**[‡], **Alexander J. Sercel**[‡], **Madeleine F. Shade**[‡], **Stuart C. Feinstein**[‡], **Michael T. Bowers**[†], and **Joan-Emma Shea**[*,†,¶]

[†]Department of Chemistry and Biochemistry, University of California at Santa Barbara, Santa Barbara, California, 93106, USA

[‡]Neuroscience Research Institute and Department of Molecular, Cellular and Developmental Biology, University of California at Santa Barbara, Santa Barbara, California, 93106, USA

[¶]Department of Physics, University of California at Santa Barbara, Santa Barbara, California, 93106, USA

Abstract

Self-aggregation of the microtubule-binding protein Tau reduces its functionality and is tightly associated with Tau-related diseases, termed tauopathies. Tau aggregation is also strongly associated with two nucleating six-residue segments, namely PHF6 (VQIVYK) and PHF6* (VQIINK). In this paper, using experiments and computational modeling, we study the self-assembly of individual and binary mixtures of Tau fragments containing PHF6* (R2/wt; ^{273}GKVQIINKKLDL^{284}) and PHF6 (R3/wt; ^{306}VQIVYKPVDLSK^{317}), and a mutant R2/ΔK280 associated with a neurodegenerative tauopathy. The initial stage of aggregation is probed by ion-mobility mass spectrometry, the kinetics of aggregation monitored with Thioflavin T assays and the morphology of aggregates visualized by transmission electron microscopy. Insights into the structure of early aggregates and the factors stabilizing the aggregates are obtained from replica exchange molecular dynamics simulations. Our data suggest that R3/wt has a much stronger aggregation propensity than either R2/wt or R2/ΔK280. Heterodimers containing R3/wt are less stable than R3/wt homodimers but much more stable than homodimers of R2/wt and R2/ΔK280, suggesting a possible role of PHF6*/PHF6 interactions in initiating the aggregation of full length Tau. Lastly, R2/ΔK280 binds stronger to R3/wt than R2/wt suggesting a possible mechanism for a pathological loss of normal Tau function.

[*]To whom correspondence should be addressed: shea@chem.ucsb.edu. Phone: +1 (805) 893–5604. Fax: +1 (805) 893–4102.
[§]Current address: Center for Computational and Integrative Biology and Department of Physics, Rutgers University-Camden, Camden, New Jersey 08102, USA.

Supporting Information

Supporting Information (SI) file contains supplementary figures showing aggregation of peptides monitored by Thioflavin T, linear detection range of Thioflavin T assays, arrival time distributions of R3/wt peaks in IM-MS experiments, snapshots of R3/wt homodimers with the most probable conformations obtained from molecular dynamics simulations, and distribution of hydrogen bonds in homodimers/heterodimers of R3/wt. Theoretical collision cross sections of R3/wt heterodimers are also listed. This material is available free of charge via the Internet at http://pubs.acs.org.

Notes

The authors declare no competing financial interest.

Introduction

Tau is a highly soluble, intrinsically disordered protein that normally binds to microtubules and regulates their dynamic growing and shortening behaviors.[1–3] In Alzheimer's disease (AD) and related neurodegenerative diseases, Tau dissociates from microtubules and self-associates to form abnormal fibrillar aggregates.[4,5] The distribution of these aberrant Tau structures is very well-correlated with neuronal cell death and the clinical progression of the diseases, suggesting an intimate link between aberrant Tau structure and neurodegeneration/dementia (reviewed by Binder *et al.*[6]). Recent efforts to identify the neurotoxic species of Tau have shifted focus away from mature, fibrillar aggregates toward smaller oligomeric Tau species.[7,8] Studies with antibodies that selectively recognize Tau oligomers have demonstrated that these species are elevated in AD brains.[9–11] Cell to cell transmission of oligomeric Tau and other aberrant pre-fibrillar species may underlie the spread of Tau pathology,[12–15] and these species show promise as potential therapeutic targets.[16,17] A structural understanding of early Tau aggregates may lead to a deeper understanding of their neurotoxic mechanisms, as well as to the rational design of therapeutic drugs.

As a result of alternative RNA splicing there are 6 distinct isoforms of Tau that differ from one another depending upon the presence or absence of three inserts encoded by exons 2, 3 and 10 of the Tau gene (Figure 1). There are two important domains in each Tau isoform: the N-terminal projection domain determines the inter-microtubule spacing between bundled microtubules and also mediates interactions of microtubules with plasma membrane. Exons 2 and 3 each encode 29-residue acidic inserts located in the N-terminal projection domain. In contrast, the microtubule binding pseudo-repeat (MTBR) domain contains either three or four imperfect repeats (depending upon the presence or absence of exon 10 encoded sequences) and serves to bind microtubules directly and to regulate their dynamics.[22] This same region of the protein makes up the core of fibrillar Tau aggregates,[23,24] and Tau aggregation is accompanied by a regional transition from random coil to β-sheet structure. Fibrillar Tau aggregates have a cross-β-structure typical of amyloid fibrils. Finally, the 6 tau isoforms differ from one another not only structurally but also in terms of the relative expression levels and their rates and extents of fibril formation.[18–21] Genetic evidence demonstrates unequivocally that functional differences must exist among the 6 different tau isoforms.

Experimental aggregation studies, as well as computer simulations, have identified two important nucleating sequences within the MTBR, namely PHF6 (VQIVYK) and PHF6* (VQIINK).[26,27] In vitro studies demonstrated that short Tau peptides containing PHF6 or PHF6* can form fibrillar aggregates.[28] PHF6 is located at the beginning of the third repeat and is present in all Tau isoforms. In contrast, PHF6* is located at the beginning of the second repeat and is present only in four-repeat (4R) Tau isoforms (Figure 1) since it is encoded by alternatively spliced exon 10 sequences. PHF6* is the location of the ΔK280 mutation, which deletes the lysine present in PHF6* and causes a severe form of hereditary neurodegeneration. There are at least four additional disease-related mutants near these two hexapeptides that have been shown to induce more β-strand character, impair the ability of Tau to interact with microtubules and subsequently enhance filament formation (reviewed by Goedert *et al.*[29]). Crystallographic studies of the PHF6 peptide suggest that it stacks in

parallel β-sheets within the context of a fibril, and that two mating sheets come together with their hydrophobic side chains oriented inward to form a steric zipper.[30] A parallel β-sheet arrangement of the PHF6 segment within the fibrillar core is also supported by studies using solid state NMR[31] and electron paramagnetic resonance.[32] The latter technique revealed that the arrangement of the PHF6* segment can occupy a parallel β-sheet arrangement or a disordered arrangement, and that the parallel β-sheet arrangement is strongly promoted by the ΔK280 mutation.[33,34]

Previous work from our labs used a combination of computer simulations, ion mobility mass spectrometry (IM-MS), and transmission electron microscopy (TEM) to probe the structure and aggregation of a 12-amino acid peptide encompassing PHF6* and adjacent amino acids ("R2/wt", ^{273}GKVQIINKKLDL^{284}).[35] We found that the aggregation propensity of this peptide is related to the tendency of PHF6* to adopt an extended β-sheet conformation, with this tendency being stronger in the ΔK280 mutant ("R2/ΔK280", ^{273}GKVQIIN − KLDL^{284}) than in the wild-type (wt) peptide.

The PHF6 hexapeptide can self-aggregate even in the absence of the other peptides of Tau protein.[36] A computer simulation study[37] on the self-aggregation of the PHF6 fragment found a zipper-like arrangement of the amino acid residues owing to hydrophobic stabilization, similar to that reported by Sawaya *et al.*[30] On the other hand, structural models predict that the lysine in PHF6* makes interactions between PHF6–PHF6* unfavorable;[38] however, there is evidence that these sequences do interact. To identify PHF6 binding sequences, von Bergen and colleagues generated a library of overlapping Tau peptides immobilized on a membrane, and probed the membrane with a radio-labeled Tau fragment containing PHF6. Although binding was the strongest for peptides overlapping the PHF6 sequence, they also detected substantial binding to peptides overlapping the PHF6* sequence.[39] There is also evidence that these sequences interact during aggregation. Using short peptides corresponding to PHF6 and PHF6*, Moore and colleagues found evidence of direct PHF6-PHF6* interactions by circular dichroism and Thioflavin S (ThS) fluorescence under aggregating conditions.[40] While the former two studies employed short Tau peptides, there is also evidence for PHF6–PHF6* interactions in the context of large Tau fragments. In a fragment corresponding to the MTBR region of 4R Tau, insertion of a β-sheet-disrupting proline residue into either PHF6 or PHF6* was sufficient to suppress aggregation, as measured by ThS fluorescence and TEM. Interestingly, the inhibitory effect of a proline in the PHF6 sequence was overcome, and aggregation restored, by the presence of the ΔK280 mutation in the PHF6* sequence.[28] In an even longer tau fragment composed of the 4-repeat MTBR and C-terminal tail, Peterson and colleagues used NMR to probe Tau structure during aggregation, and found data consistent with a heterogeneous population of oligomeric species in which intermolecular interactions occur between PHF6–PHF6, PHF6*–PHF6*, and PHF6–PHF6*.[41] However, since mature Tau fibers show primarily parallel, in register β-sheet contacts between PHF6–PHF6 and PHF6*–PHF6*,[31–33] the role that PHF6–PHF6* interactions play at the early stages of aggregation is not clear.

In this paper, in order to shed new light on PHF6–PHF6* interactions, we study three individual tau peptides and their binary mixtures: R2/wt (^{273}GKVQIINKKLDL^{284}, containing PHF6*), R3/wt (^{306}VQIVYKPVDLSK^{317}, containing PHF6), and R2/ΔK280

(^{273}GKVQIIN−KLDL^{284}). A schematic of these three peptides is shown in Figure 1, along with the full-length Tau isoform upon which the amino acid numbering convention is based. These fragments were originally designed and characterized by von Bergen *et al.*,[28] and interactions between R2/wt–R2/wt and R2/ΔK280–R2/ΔK280 were previously studied with computer simulations and experiments by Larini *et al.*[35] In this present study, we focus on the homodimer of R3/wt, and heterodimers composed of R3/wt–R2/wt and R3/wt–R2/ΔK280. Using a combination of experiments (IM-MS, Thioflavin T, and TEM) and replica exchange molecular dynamics (REMD) computer simulations, we investigate and compare the propensities of different peptide combinations to form oligomers. We probe the conformations of the stable oligomers, and the molecular mechanisms responsible for stabilization. We also discuss the effect of the ΔK280 mutation on PHF6–PHF6* interactions by comparing the results obtained with R2/wt and R2/ΔK280 peptides.

Materials and Methods

Sample preparation

The R2/wt, R2/ΔK280 and R3/wt peptides (> 98% purity) were purchased from Genscript Corp. (Piscataway, NJ), with N- and C-termini capped by acetylation and amidation, respectively. Fresh peptide powders were dissolved in water (HPLC grade; JT Baker) or 20 mM ammonium acetate buffer (pH = 7.0) to desired concentrations required for experiments.

Thioflavin T Assays and TEM

A stock solution of Thioflavin T (ThT; Anaspec) was prepared in 200 proof ethanol (Arcos Organics). Peptides stocks were prepared at 200 μM from lyophilized powder in 20 mM ammonium acetate buffer and then further diluted into the same buffer containing 2.2 μM ThT. Individual peptides were assayed at 50 μM (Supporting Information, Figure S1) and 25 μM. In binary mixtures, each peptide was present at 25 μM (50 μM total). The ThT response is linear under these conditions (Supporting Information, Figure S2). Following an initial "pre-heparin" measurement, heparin (Sigma, product H5515) was added to a final heparin to tau molar ratio of 1:4. Over the next 24 h, ThT fluorescence was monitored at 450ex/510em using a Wallac 1420 plate reader spectrofluorometer (PerkinElmer). After 24 h, samples of each aggregation mixture were removed and prepared for TEM. Briefly, samples were fixed in glutaraldehyde (1.6% final; Electron Microscopy Sciences), placed on 300-mesh formvar-carbon coated copper grids (Electron Microscopy Sciences), and then negatively stained with 2% uranyl acetate. Grids were imaged via a JEOL 1230 microscope equipped with an ORCA camera driven by AMT Image Capture Software (Version 5.24).

Ion Mobility Mass Spectrometry

Sample preparation—The peptide powders were dissolved in water to the concentration of 500 μM. Prior to IM-MS experiments, the stock solutions were diluted to 50 μM. For the binary mixtures of the peptides, the concentration of each peptide was 25 μM, so that the total peptide concentration was kept the same for all samples.

IM-MS experiments—The IM-MS instrument was built in-house and consists of a nano-ESI source, an ion funnel, a 200-cm long drift cell and a quadrupole mass filter.[42] In the experiments, ions were generated through means of nano-ESI, stored in a source funnel and subsequently pulsed into a drift cell filled with helium gas at high pressure. The ions drift through the cell with a constant velocity due to the effects of a weak electrical field and a drag force resulting from the collisions with the buffer gas molecules. The arrival time distributions (ATDs) of mass-selected ions can be measured at different drift voltages, and subsequently used to determine the reduced mobility K_0. The experimental cross sections of specific species can be calculated from K_0 after the oligomer size n and the charge z are assigned, as shown in Eq. 1[43,44]

$$\sigma_{exp} \approx \Omega_{avg} = \frac{(18\pi)^{1/2}}{16}\left[\frac{1}{m}+\frac{1}{m_b}\right]^{1/2}\frac{ze}{(k_B T)^{1/2}}\frac{1}{K_0}\frac{1}{N} \quad (1)$$

where m and m_b are the molecular weights of the ions and buffer gas molecules, respectively, ze is the charge of the ion, N is the buffer gas density and Ω_{avg} is the average collision cross section integral, which approximates the average collision cross section σ. Collision cross sections of theoretical structures obtained from simulations are computed using the Projection Approximation Method (PSA) available from http://luschka.bic.ucsb.edu:8080/WebPSA/.[45,46]

Molecular dynamics simulations

All-atomistic molecular simulations were performed using the GROMACS 4.5.5 package,[47] and a combination of the OPLS-AA[48–50] force field for protein and TIP3P[51] model for water. All the bonds of the peptide chains were constrained using the LINCS algorithm[52] and the water molecules were kept fully rigid using the SETTLE algorithm.[53] All the peptides were simulated in their natural charged states. The net positive charges on protein were neutralized with the addition of the chloride ions. The long range electrostatic interactions were calculated using the particle mesh Ewald method[54] with a grid spacing of 0.12 nm. The direct space cut-off radius for all nonbonded interactions was 1.2 nm. The Newtonian equations of motion were integrated using leap-frog integrator[55] with a time step of 2 fs. Molecular trajectories were sampled using replica exchange molecular dynamics (REMD)[56–58] scheme with canonical NVT ensemble. For the systems containing mixed R2 (R2/wt and R2/ΔK280) and R3/wt chains, a temperature range of 290 K to 450 K was sampled using 60 replicas. A temperature range of 290 K to 490 K was explored using 63 replicas for R3/wt homodimers. For every temperature used for exchanging the replicas, Nosé-Hoover thermostat[59,60] was used to keep the temperature constant. The replicas were exchanged every 3 ps with an average exchange probability of 20–25%. Trajectories were accumulated for 200–400 ns preceded by 100–150 ns of equilibration and the data obtained at 300 K were used for the analyses.

The conformations of the peptide chains were grouped by performing a cluster analysis based on the Daura algorithm.[61] The root mean square deviations (RMSD) of the peptide backbones were calculated and the conformations were grouped together if the RMSD of the peptide backbones were less than 0.26 nm compared to each other. Criteria for identifying a

hydrogen bond were: (a) the distance between the oxygen and the hydrogen atom must be less than 0.25 nm and (b) the angle defined by oxygen-hydrogen-donor must be less than 30°. The end-to-end distance (R_{ee}) of the peptide chains were calculated by measuring the distance between the centers of mass of the acetylated and the amidated termini. The relative orientations of the monomers in a dimer were calculated by measuring the angles between the vectors connecting the alpha-carbons of V275 and K280 (for R2/wt), V275 and K281 (for R2/ΔK280), and I308 and V313 (for R3/wt). All the analyses were performed using the standard GROMACS tools.

Results and Discussion

R3/wt has a higher aggregation propensity than either R2/wt or R2/ΔK280

The mass spectra of R3/wt and the binary mixtures are shown in Figure 2, panel A. Each peak is annotated with *n/z* where *n* is oligomer size and *z* is the charge. As seen in Figure 2A, in addition to the R3/wt monomer peak with a charge state *z* = +2, oligomers larger than trimers can be unambiguously observed in the mass spectrum and ion-mobility data. Ion-mobility experiments reveal the existence of oligomers as large as octamers (see Supporting Information, Figure S3). The ATD of *n/z* = 2/3 contains multiple dimer features with compact to extended conformations (see also Figure 4A). The ATD of *n/z* = 3/4 contains multiple trimer features. The ATD of *n/z* = 1/1 contains features corresponding to tetramer, hexamer and octamer. The assignment of the features is based on a combination of the isotropic model (which approximates the size of the globular oligomers)[62] and the arrival time differences between features under an assumption that the relative contribution of a monomer chain to the cross section decreases as the oligomer grows in size. The oligomer peaks in the mass spectra involving R3/wt peptides are significantly more intense than those of R2/wt and R2/ΔK280 obtained under the same condition (data not shown), suggesting that R3/wt is more prone to oligomerization than the other two peptides previously investigated.[35] However, the signal to noise (S/N) is high for high *m/z* species at longer incubation time, suggesting that there is not significant fibril formation as observed in self-aggregating, fibril formation peptides.[63] These results are in good agreement with the ThT assay, as elaborated below.

The kinetics of β-sheet oligomers and fibril formation in the first 6 hours in the presence and absence of heparin, a polyanionic compound that greatly stimulates Tau aggregation, is monitored with ThT assays (see Figure 3 and Supporting Information Figure S1 for 24-hour data). In the presence of heparin (panel A), R3/wt aggregates rapidly during which the kinetics show a rapid initial rise followed by a sigmoidal phase, and the ThT signal plateaus an order of magnitude higher than in the case of R2/wt or R2/ΔK280 (see Figure S1, panel A). Of the latter two peptides, R2/ΔK280 shows the fastest aggregation. R2/wt aggregation is slower and follows a lag phase, but the ThT signal eventually reaches a higher plateau than in the case of the R2/ΔK280 mutant. In the absence of heparin (Figure 3, panel B), only ThT signals of the R3/wt sample show a significant rise. However, since the maximum ThT intensity after 24 hours in the absence of heparin is only half of that in the presence of heparin (see Figure S1), and TEM imaging shows no abundant fibril formation of R3/wt without heparin (up to 50 μM, data not shown), we conclude that R3/wt fibril formation

takes much longer than 24 hours. Within this time frame, only β-rich oligomers and protofibrils can be formed, which is also consistent with the detection up to octamer by IM-MS mentioned before.

R3/wt forms stable heterodimers with R2/wt and R2/ΔK280 suggesting possible interactions between the second and third repeats of full length Tau

We examine binary mixtures of R3/wt–R2/wt, R3/wt–R2/ΔK280, and R2/wt–R2/ΔK280 with IM-MS (see Figure 2B–D). In all cases, mass spectral peaks corresponding to heterodimers are observed. We first consider the homo- and heterodimers of R2/wt and R2/ΔK280, and use them as calibrants to better evaluate the stability of heterodimers containing R3/wt. A previous study[35] of R2/wt and R2/ΔK280 utilizing the same theoretical and experimental approach indicated that R2/ΔK280 supports a slightly better packing of homodimer configurations than R2/wt, due to the absence of a bulky, charged lysine. However, their homodimers are not significantly different in terms of stability. That conclusion is confirmed in the mass spectrum of the R2/wt and R2/ΔK280 mixture, in which the peak intensity ratio of homo-R2/ΔK280:heterodimer:homo-R2/wt is very close to 1:2:1 expected for statistical assembly. That is, heterodimers can exist in AB or BA configurations, as compared to a unique configuration AA or BB of the homodimers; therefore, the 1:2:1 ratio solely reflects that the possibility of dimer formation is twice the possibility for each homodimer to be formed, independently of structural stability. On the other hand, the corresponding ratios for binary mixtures containing R3/wt are not 1:2:1. They show a monotonic increase going from non-R3/wt homodimers, heterodimers to R3/wt homodimers. Therefore, the mass spectral data suggest that R3/wt homodimers are not only more stable than the homodimers of the other two peptides, but its heterodimers are also more favored to form than the R2/wt and R2/ΔK280 homodimers. This conclusion is in agreement with our REMD simulations showing that both R2 peptides form very stable dimers with R3/wt, even at ≈ 450K. For comparison, a dimer that contains only R2 peptides (either R2/wt or R2/ΔK280 homodimers) is stable up to ≈ 360K.[35] Furthermore, our simulation studies also show stable homodimer formation for R3/wt peptide at 490K (higher than that of the heterodimers). This result is in excellent agreement with the IM-MS and the ThT data, revealing the high aggregation propensity of R3/wt and stability of its homodimers over the heterodimers and R2/wt-containing homodimers.

The ATDs of the R3/wt homo- and heterodimer peaks are shown in Figure 4. These data indicate that both R3/wt homo- and heterodimers can adopt both extended conformations (shown in red) and compact conformations (shown in blue). The extended conformations have higher populations, as shown by the intensities of the features at longer arrival times. Homodimers of R3/wt (panel A) contain a higher populations of extended structures than the two heterodimers (panels B–C). The experimental cross sections for the R3/wt homo- and heterodimers are in reasonably good agreement with those of the structures obtained from REMD simulations discussed below (see Figure S3 and Table S1 in the Supporting Information). Since no heteroligomers larger than dimer are observed, the competitive dimerization between R3/wt homo- and heterodimers may underlie an inhibition of R3/wt aggregation as observed by the ThT assays when R2/wt or R2/ΔK280 is present, as shown by comparing data in Figure 5 and Figure 3 (and also Figure S1).

The ThT signals of binary mixtures show that in each case aggregation is inhibited. The R2/wt–R2/ΔK280 mixture follows the same trends as R2/ΔK280 alone under the same condition (with or without heparin). However, the extent of R2/wt–R2/ΔK280 aggregation is less than R2/wt alone, despite the fact that the total peptide concentration in the binary mixture is twice as high.

R3/wt aggregation is in general inhibited in the presence of either R2 peptide. In detail, in the presence of heparin (panel A), the R3/wt–R2/ΔK280 mixture aggregates rapidly with two apparent phases, similar to R3/wt alone, but always at a lower level. The lag phases of aggregation are also prolonged. Aggregation in the R3/wt–R2/wt mixture is initially slower than R3/wt–R2/ΔK280 but reaches a high plateau. In the absence of heparin (panel B), R3/wt aggregation is completely suppressed by R2/ΔK280. In the absence of heparin, R3/wt aggregation is delayed by R2/wt, but eventually reaches the same plateau as in the case of pure R3/wt (see Figure 3, panel B). The overall ThT data indicate that the interactions of R3/wt and R2 containing peptides are significant enough to slow down the aggregation. We conclude that R3/wt interacts more strongly with R2/ΔK280 than R2/wt (as shown in panel B), although the data in the presence of heparin (panel A) are ambiguous. Perhaps in the presence of heparin the aggregation kinetics are dominated by how each peptide interacts with heparin rather than their binary interactions.

Figure 6 shows the fibril morphologies of individual peptides and their binary mixtures incubated for 24 hours in the presence of heparin. All samples populate fibrillar aggregates with diverse morphologies, including twisted fibers, ribbons, and bundles. Twisted fibrils are especially common for R2/wt whereas bundles are abundant in the case of R2/ΔK280. The formation of fibrils in R3/wt containing mixtures suggests that although the interactions of R3/wt with the other two peptides are strong, the inhibition effect is overcome by interactions with heparin and the preference of R3/wt oligomers over heteroligomers.

PHF6–PHF6 and PHF6–PHF6* interactions are stronger than PHF6*–PHF6* interactions: Molecular mechanism behind the stability

Experiments indicate interactions containing R3/wt (i.e. PHF6) either with itself or R2/wt or R2/ΔK280 are favored. Consequently, we will focus on the R3/wt homo- and heterodimers in our REMD simulations. A cluster analysis based on the Daura algorithm[61] of the different peptide conformations suggests a wide range of possible dimer structures. Relevant representational conformations with significant populations are shown in Figure S4 in the Supporting Information. In order to analyze the structures and the conformations quantitatively we have plotted the distribution of the radius of gyration (R_g) of the dimers against the reduced end-to-end distance (R_r) of the dimers, where the reduced end-to-end distance of the dimers is defined as $R_r = \sqrt{R_{ee1}^2 + R_{ee2}^2}$ with R_{eeN} being the end-to-end distance of the N-th chain. The corresponding conformational distributions are shown in Figure 7. Panels A, B and C show the distributions of R_g and R_r for R2/wt–R3/wt, R2/ΔK280–R3/wt and R3/wt–R3/wt dimers, respectively. The distributions of both compact and extended structures in the three systems are consistent with the ion-mobility data shown in Figure 4. According to the simulation data, R2/ΔK280–R3/wt heterodimers predominantly prefer extended conformations (R_g > 0.9 nm) with both peptide chains adopting strand-like

structures (i.e. panel E showing both chains with $R_{ee} \geq 3$nm whereas the R2/wt–R3/wt heterodimers and the R3/wt homodimers explore both extended and compact conformations ($R_g < 0.9$ nm), with R3/wt homodimers being relatively more ordered than R2/wt–R3/wt dimers (panels F vs. D). This observation is in good agreement with the experimental data suggesting that R2/ΔK280 is better at interacting with R3/wt to inhibit aggregation.

We also determined the relative orientations (parallel/anti-parallel vs. disordered) of the individual chains within a dimer with respect to each other by calculating the angles between the peptide chains as described in the method section. Heterodimers of R2/wt and R3/wt peptides, as plotted in Figure 8, populate broader distributions between parallel ($\cos\theta \approx 1.0$) and antiparallel ($\cos\theta \approx -1.0$) conformations as compared to the R2/ΔK280–R3/wt and R3/wt–R3/wt dimers. The antiparallel orientations are slightly more preferred over the parallel conformations for both heterodimers. In contrast, R3/wt homodimers are much more ordered in terms of the relative orientations of the monomer chains, with parallel orientations preferred. For comparison, it can be mentioned that the dimers consisting of only R2 peptides show primarily antiparallel conformations. This preference was stronger in R2/wt homodimers than in R2/ΔK280 homodimers.[35] The effect of parallel vs. anti-parallel arrangements within β-rich oligomers on fibril formation has attracted attentions in recent years. In general, peptides that promote anti-parallel alignment tend to have slower aggregation kinetics than parallel-aligned peptides, supported by several classes of steric zipper x-ray structures solved by Eisenberg and co-workers.[30] The underlying phenomenon is that parallel alignment allows an easier matching between mating β-sheets to form a steric zipper, a type of oligomer that is crucial for fibril formation. Thus, the peptide chain alignment within R3/wt dimers (i.e. parallel) is consistent with its strong aggregation propensity, while that of R2/wt and R2/ΔK280 (i.e. anti-parallel) shows a less prone behavior.

The remaining question is whether R3/wt can access favorable interactions promoting oligomer formation that are not available to both R2 peptides. An insight from MD structural analysis reveals that the formation of multiple stable hydrogen bonds between the peptide chains promotes the stability of the dimers. Figure 9, panels A–C show the distributions of the number of the hydrogen bonds between the peptide monomers for R2/wt–R3/wt, R2/ΔK280–R3/wt, and R3/wt-R3/wt dimers respectively. R3/wt peptides form four or more hydrogen bonds with R2/wt, R2/ΔK280 and R3/wt peptides in more than 85%, 90%, and 95% of the total dimer structures respectively. In comparison, R2 peptide homodimers form four or more hydrogen bonds in 10–20% of the dimer structures.[35]

We also performed a detailed analysis of the formation of hydrogen bonds between individual amino acid residues. The results are plotted in terms of the percentage of the total simulation time in Figure 9, panels D–F. From these plots, we can see that the pattern of hydrogen bonding is the most ordered in R3/wt homodimers, and the least ordered in R2/wt–R3/wt heterodimers, with R2/ΔK280–R3/wt heterodimers intermediate. It can be inferred that the PHF6 fragment in the R3/wt peptide plays a prominent role in the formation of stable hydrogen bonds, and interacts preferentially with the PHF6* fragments in the heterodimers and with the PHF6 fragment in the homodimer. The total number of PHF6–PHF6 hydrogen bonds is higher than that for PHF6–PHF6*. The number of the hydrogen

bonds between PHF6 and PHF6* contributes to the 49% of the total hydrogen bonds formed between R3/wt and R2/wt and and 57% between R3/wt and R2/ΔK280 peptides. PHF6–PHF6 hydrogen bonds contribute 59% of the total hydrogen bonds found in R3/wt homodimers. From Figure 9, panel F it is clear that the major R3/wt residues involved in hydrogen bonding are the glutamine (Q307), valine (V309), and lysine (K311) located within the PHF6 fragment. Preferential hydrogen bonding between PHF6–PHF6 and PHF6–PHF6* positions the hydrophobic sections of both peptides in close proximity. In addition, charges of opposite signs are generally close to each other in R3/wt containing dimers, adding to their stability. Furthermore, the C–H π interaction between isoleucine (I308) and tyrosine (Y310) is an essential factor contributing to the formation of the dry interface of the steric zipper oligomers.[36,64] Thus the dimers involving R3/wt peptide are more stable and ordered than the dimers composed of R2 peptides only. Comparing the two heterodimers, R3/wt–R2/ΔK280 dimers show more stability and order than R3/wt–R2/wt dimers. Homodimers composed of R2/wt chains position lysines K280 and K281 (located near the middle of the peptide) in close contact, and the resulting electrostatic repulsion destabilizes the dimer. Whereas this problem is not as prominent in the case of R2/ΔK280 homodimers.

Summary and Conclusions

We have used a variety of complementary experimental and computer simulation methods to study the interactions between PHF6 and PHF6* in the context of the short Tau peptides R3/wt, R2/wt, and R2/ΔK280. The main conclusions can be summarized as follows:

- R3/wt forms fibrillar aggregates more readily than the R2/wt or R2/ΔK280 peptides.
- The presence of either of the R2 peptides inhibits R3/wt aggregation. The R3/wt fragment binds stronger to R2/ΔK280.
- R3/wt prefers to form R3/wt–R3/wt homodimers, but also forms stable heterodimers of R3/wt–R2/wt and R3/wt–R2/ΔK280. The heterodimers containing R3/wt are more stable than R2/wt and R2/ΔK280 homodimers. In contrast, R2/wt–R2/ΔK280 heterodimers are comparable in stability to their homodimers.
- R3/wt homodimers prefer parallel conformations stabilized by PHF6–PHF6 hydrogen bonds and hydrophobic contacts. Heterodimers of R3/wt–R2/wt and R3/wt–R2/ΔK280 are less ordered in comparison, populating both parallel and antiparallel arrangements, and are stabilized by PHF6-PHF6* interactions. Of the two heterodimers, R3/wt–R2/wt are the least ordered, due to the disruptive influence of K280. Parallel alignment supports the strong aggregation propensity of R3/wt.

Taken together, our data strongly indicate the importance of PHF6, which is present in both 3R and 4R tau, as the major nucleating sequence driving Tau aggregation. PHF6 is found to play a dominant role over PHF6* (which is present in only 4R Tau) in terms of initiating and stabilizing the Tau aggregates. We suggest that this dominance is due to the strong tendency of the PHF6 sequence to populate ordered dimers with a parallel arrangement, even in the absence of aggregation inducers. In this experimental system, we find that although PHF6–

PHF6* readily interact, they result in less ordered dimer conformations than PHF6–PHF6 interactions, and are less favorable toward aggregation. It has been shown that for 3R and 4R Tau with the same N-terminal projection domain, 4R isoforms often have lower critical concentration and shorter lag time for aggregation. Interestingly, 4R Tau isoforms have been shown to drive aggregation of 3R Tau,[65] as well as 3R Tau isoforms can seed aggregation of 4R Tau,[66] suggesting possible interactions between heterotypic aggregation prone segments within 4R and 3R, in which PHF6 and PHF6* are the two strongest candidates. Our data unambiguously strengthen this hypothesis, as the interactions can become more favorable when both segments are present in the same protein sequence (for example, by promoting a favorable arrangement of the intervening and surrounding sequences). Our data support models in which many structural rearrangements accompany the transition from dimers and early oligomers to mature fibers.[37] Molecular mechanisms behind the interactions involving PHF6 and PHF6*, as inferred from our results, can potentially explain the physical nature of the aggregation of full-length 3R and 4R Tau proteins. Furthermore, the strong binding between R3/wt with disease related ΔK280 mutant implies a possible toxicity mechanism, as the tight complexes of PHF6 containing Tau and the ΔK280 mutant could reduce the population of functional Tau available to regulate microtubule dynamics and/or to promote pathological trans-synaptic tau transfer.

Supplementary Material

Refer to Web version on PubMed Central for supplementary material.

Acknowledgments

Support from the National Science Foundation MCB-1158577 (J.-E.S), CHE-1301032 (M.T.B), the National Institute of Health grant number 1RO1AG047116-01 (M.T.B) and the David and Lucile Packard Foundation (J.-E.S) are gratefully acknowledged, as well as a Special Santa Barbara Cottage Hospital-UCSB Research Award (N.E.L). This work used the Extreme Science and Engineering Discovery Environment (XSEDE), which is supported by National Science Foundation grant number OCI-1053575. The authors acknowledge the Texas Advanced Computing Center (TACC) at University of Texas at Austin and the National Institute for Computational Sciences at Oak Ridge National Laboratory for providing HPC resources through the XSEDE grant number TG-MCA05S027. This research used ShaRCS, UC Shared Research Computing Services Cluster, which is technically supported by multiple UC IT divisions and managed by the University of California, Office of the President. We acknowledge support from the Center for Scientific Computing at the CNSI and MRL: an NSF MRSEC (DMR-1121053) and NSF CNS-0960316. We also acknowledge the use of the NRI-MCDB Microscopy Facility at UC, Santa Barbara.

References

1. Desai A, Mitchison TJ. Microtubule Polymerization Dynamics. Annu Rev Cell Dev Biol. 1997; 13:83–117. [PubMed: 9442869]
2. Conde C, Cáceres A. Microtubule Assembly, Organization and Dynamics in Axons and Dendrites. Nat Rev Neurosci. 2009; 10:319–332. [PubMed: 19377501]
3. Nogales E. Structural Insights into Microtubule Functions. Annu Rev Biochem. 2000; 69:277–302. [PubMed: 10966460]
4. Braak H, Braak E. Frequency of Stages of Alzheimer-Related Lesions in Different Age Categories. Neurobiol Aging. 1997; 18:351–357. [PubMed: 9330961]
5. Johnson GV, Jenkins SM. Tau Protein in Normal and Alzheimer's Disease Brain. Alz Dis Rev. 1996; 1:38–54.
6. Binder LI, Guillozet-Bongaarts AL, Garcia-Sierra F, Berry RW. Tau, Tangles, and Alzheimer's Disease. Biochim Biophys Acta. 2005; 1739:216–223. [PubMed: 15615640]

7. Flach K, Hilbrich I, Schiffmann A, Gärtner U, Krüger M, Leonhardt M, Waschipky H, Wick L, Arendt T, Holzer M. Tau Oligomers Impair Artificial Membrane Integrity Cellular Viability. J Biol Chem. 2012; 287:43223–43233. [PubMed: 23129775]
8. Lasagna-Reeves CA, Castillo-Carranza DL, Guerrero-Muoz MJ, Jackson GR, Kayed R. Preparation Characterization of Neurotoxic Tau Oligomers. Biochemistry. 2010; 49:10039–10041. [PubMed: 21047142]
9. Lasagna-Reeves CA, Castillo-Carranza DL, Sengupta U, Sarmiento J, Tron-coso J, Jackson GR, Kayed R. Identification of Oligomers at Early Stages of Tau Aggregation in Alzheimer's Disease. FASEB J. 2012; 26:1946–1959. [PubMed: 22253473]
10. Patterson KR, Remmers C, Fu Y, Brooker S, Kanaan NM, Vana L, Ward S, Reyes JF, Philibert K, Glucksman MJ, Binder LI. Characterization of Prefibrillar Tau Oligomers in Vitro in Alzheimer Disease. J Biol Chem. 2011; 286:23063–23076. [PubMed: 21550980]
11. Ward SM, Himmelstein DS, Lancia JK, Fu Y, Patterson KR, Binder LI. TOC1: Characterization of a Selective Oligomeric Tau Antibody. J Alzheimers Dis. 2013; 37:593–602. [PubMed: 23979027]
12. Lasagna-Reeves CA, Castillo-Carranza DL, Sengupta U, Guerrero-Munoz MJ, Kiritoshi T, Neugebauer V, Jackson GR, Kayed R. Alzheimer Brain-derived Tau Oligomers Propagate Pathology from Endogenous Tau. Sci Rep. 2012; 2:700. [PubMed: 23050084]
13. Frost B, Jacks RL, Diamond MI. Propagation of Tau Misfolding from the Outside to the Inside of a Cell. J Biol Chem. 2009; 284:12845–12852. [PubMed: 19282288]
14. Wu JW, Herman M, Liu L, Simoes S, Acker CM, Figueroa H, Stein-berg JI, Margittai M, Kayed R, Zurzolo C, Di Paolo G, Duff KE. Small Misfolded Tau Species are Internalized via Bulk Endocytosis and Anterogradely and Retrogradely Transported in Neurons. J Biol Chem. 2013; 288:1856–1870. [PubMed: 23188818]
15. Kfoury N, Holmes BB, Jiang H, Holtzman DM, Diamond MI. Trans-cellular Propagation of Tau Aggregation by Fibrillar Species. J Biol Chem. 2012; 287:19440–19451. [PubMed: 22461630]
16. Castillo-Carranza DL, Gerson JE, Sengupta U, Guerrero-Munoz MJ, Lasagna-Reeves CA, Kayed R. Specific Targeting of Tau Oligomers in Htau Mice Prevents Cognitive Impairment and Tau Toxicity Following Injection with Brain-derived Tau Oligomeric Seeds. J Alzheimers Dis. 2014; 40(Suppl 1):S97–S111. [PubMed: 24603946]
17. Castillo-Carranza DL, Sengupta U, Guerrero-Munoz MJ, Lasagna-Reeves CA, Gerson JE, Singh G, Estes DM, Barrett ADT, Dineley KT, Jackson GR, Kayed R. Passive Immunization with Tau Oligomer Monoclonal Antibody Re verses Tauopathy Phenotypes without Affecting Hyperphosphorylated Neurofibrillary Tangles. J Neurosci. 2014; 34:4260–4272. [PubMed: 24647946]
18. Liu F, Gong C-X. Tau Exon 10 Alternative Splicing and Tauopathies. Mol Neurode-generation. 2008; 3:8.
19. Hartmann AM, Rujescub D, Giannakourosc T, Nikolakakic E, Goedertd M, Mandelkowe E-M, Gaof QS, Andreadisf A, Stamma S. Regulation of Alternative Splicing of Human Tau Exon 10 by Phosphorylation of Splicing Factors. Mol Cell Neurosci. 2001; 18:80–90. [PubMed: 11461155]
20. Varani L, Hasegawa M, Spillantini MG, Smith MJ, Murrell JR, Ghetti B, Klug A, Goedert M, Varani G. Structure of Tau Exon 10 Splicing Regulatory Element RNA and Destabilization by Mutations of Frontotemporal Dementia and Parkinsonism Linked to Chromosome 17. Proc Natl Acad Sci U S A. 1999; 96:8229–8234. [PubMed: 10393977]
21. Siddiqua A, Luo Y, Meyer V, Swanson MA, Yu X, Wei G, Zheng J, Eaton GR, Ma B, Nussinov R, Eaton SS, Margittai M. Conformational Basis for Asymmetric Seeding Barrier in Filaments of Three- Four-Repeat Tau. J Am Chem Soc. 2012; 134:10271–10278. [PubMed: 22656332]
22. Lee G, Neve RL, Kosik KS. The Microtubule Binding Domain of Tau Protein. Neuron. 1989; 2:1615–1624. [PubMed: 2516729]
23. Novak M, Kabat J, Wischik CM. Molecular Characterization of the Minimal Protease Resistant Tau Unit of the Alzheimer's Disease Paired Helical Filament. EMBO J. 1993; 12:365–370. [PubMed: 7679073]
24. von Bergen M, Barghorn S, Muller SA, Pickhardt M, Biernat J, Mandelkow E-M, Davies P, Aebi U, Mandelkow E. The Core of Tau-paired Helical Filaments Studied by Scanning Transmission

Electron Microscopy and Limited Proteolysis. Biochemistry. 2006; 45:6446–6457. [PubMed: 16700555]

25. von Bergen M, Barghorn S, Biernat J, Mandelkow E-M, Mandelkow E. Tau Aggregation is Driven by a Transition from Random Coil to β-Sheet Structure. Biochim Biophys Acta, Mol Basis Dis. 2005; 1739:158–166.
26. Li W, Lee VM. Characterization of Two VQIXXK Motifs for Tau Fibrillization in Vitro. Biochemistry. 2006; 45:15692–15701. [PubMed: 17176091]
27. Luo Y, Ma B, Nussinov R, Wei G. Structural Insight into Tau Protein's Paradox of Intrinsically Disordered Behavior, Self-Acetylation Activity, and Aggregation. J Phys Chem Lett. 2014; 5:3026–3031. [PubMed: 25206938]
28. von Bergen M, Barghorn S, Li L, Marx A, Biernat J, Mandelkow E-M, Mandelkow E. Mutations of Tau Protein in Frontotemporal Dementia Promote Aggregation of Paired Helical Filaments by Enhancing Local β-Structure. J Biol Chem. 2001; 276:48165–48174. [PubMed: 11606569]
29. Goedert M, Jakes R. Mutations Causing Neurodegenerative Tauopathies. Biochim Biophys Acta. 2005; 1739:240–250. [PubMed: 15615642]
30. Sawaya MR, Sambashivan S, Nelson R, Ivanova MI, Sievers SA, Apostol MI, Thompson MJ, Balbirnie M, Wiltzius JJ, McFarlane HT, Madsen AØ, Riekel C, Eisenberg D. Atomic Structures of Amyloid Cross-β Spines Reveal Varied Steric Zippers. Nature. 2007; 447:453–457. [PubMed: 17468747]
31. Daebel V, Chinnathambi S, Biernat J, Schwalbe M, Habenstein B, Loquet A, Akoury E, Tepper K, Müller H, Baldus M, Griesinger C, Zweckstetter M, Mandelkow E, Vijayan V, Lange A. Beta-Sheet Core of Tau Paired Helical Filaments Revealed by Solid-state NMR. J Am Chem Soc. 2012; 134:13982–13989. [PubMed: 22862303]
32. Margittai M, Langen R. Template-assisted Filament Growth by Parallel Stacking of Tau. Proc Natl Acad Sci U S A. 2004; 101:10278–10283. [PubMed: 15240881]
33. Margittai M, Langen R. Side Chain-dependent Stacking Modulates Tau Filament Structure. J Biol Chem. 2006; 281:37820–37827. [PubMed: 17023423]
34. Meyer V, Dinkel PD, Luo Y, Yu X, Wei G, Zheng J, Eaton GR, Ma B, Nussinov R, Eaton SS, Margittai M. Single Mutations in Tau Modulate the Populations of Fibril Conformers through Seed Selection. Angew Chem Intl Ed. 2014; 53:1590–1593.
35. Larini L, Gessel MM, LaPointe NE, Do TD, Bowers MT, Feinstein SC, Shea J-E. Initiation of Assembly of Tau(273–284) and Its ΔK280 Mutant: An Experimental and Computational Study. Phys Chem Chem Phys. 2013; 15:8916–8928. [PubMed: 23515417]
36. Goux WJ, Kopplin L, Nguyen AD, Leak K, Rutkofsky M, Shanmuganandam VD, Sharma D, Inouye H, Kirschner DA. The Formation of Straight and Twisted Filaments from Short Tau Peptides. J Biol Chem. 2004; 279:26868–26875. [PubMed: 15100221]
37. Li DW, Mohanty S, Irbäck A, Huo S. Formation and Growth of Oligomers: A Monte Carlo Study of an Amyloid Tau Fragment. PLOS Comput Biol. 200810.1371/journal.pcbi.1000238
38. Wang W, Hecht MH. Rationally Designed Mutations Convert de novo Amyloid-like Fibrils into Monomeric β-sheet Proteins. Proc Natl Acad Sci U S A. 2002; 99:2760–2765. [PubMed: 11880628]
39. von Bergen M, Friedhoff P, Biernat J, Heberle J, Mandelkow E. Assembly of Tau Protein into Alzheimer Paired Helical Filaments Depends on a Local Sequence Motif (306VQIVYK311) Forming β Structure. Proc Natl Acad Sci U S A. 2000; 97:5129–5134. [PubMed: 10805776]
40. Moore CL, Huang MH, Robbennolt SA, Voss KR, Combs B, Gamblin TC, Goux WJ. Secondary Nucleating Sequences Affect Kinetics and Thermodynamics of Tau Aggregation. Biochemistry. 2011; 50:10876–10886. [PubMed: 22085312]
41. Peterson DW, Zhou H, Dahlquist FW, Lew J. A Soluble Oligomer of Tau Associated with Fiber Formation Analyzed by NMR. Biochemistry. 2008; 47:393–7404.
42. Kemper PR, Dupuis NF, Bowers MT. A New, Higher Resolution, Ion Mobility Mass Spectrometer. Int J Mass Spectrom. 2009; 287:46–57.
43. Mason, EA. Transport Properties of Ions in Gases. 99. John Wiley & Sons; 1988.

44. Gidden J, Ferzoco A, Baker ES, Bowers MT. Duplex Formation and the Onset of Helicity in Poly d(CG)n Oligonucleotides in a Solvent-Free Environment. J Am Chem Soc. 2004; 126:15132–15140. [PubMed: 15548010]
45. Bleiholder C, Wyttenbach T, Bowers MT. A Novel Projection Approximation Algorithm for the Fast and Accurate Computation of Molecular Collision Cross Sections (I). Method. Int J Mass Spectrom. 2011; 308:1–10.
46. Bleiholder C, Contreras S, Do TD, Bowers MT. A Novel Projection Approximation Algorithm for the Fast and Accurate Computation of Molecular Collision Cross Sections (II). Parameterization and Application to Biomolecules. Int J Mass Spectrom. 2013:345–347.
47. Hess B, Kutzner C, van der Spoel D, Lindahl E. GROMACS 4: Algorithms for Highly Efficient, Load-Balanced, and Scalable Molecular Simulation. J Chem Theory Comput. 2008; 4:435–447.
48. Jorgensen WL, Maxwell DS, Tirado-Rives J. Development and Testing of the OPLS All-Atom Force Field on Conformational Energetics and Properties of Organic Liquids. J Am Chem Soc. 1996; 118:11225–11236.
49. Rizzo RC, Jorgensen WL. OPLS All-Atom Model for Amines: Resolution of the Amine Hydration Problem. J Am Chem Soc. 1999; 121:4827–4836.
50. Kaminski GA, Friesner R, Tirado-Rives J, Jorgensen WL. Evaluation and Reparametrization of the OPLS-AA Force Field for Proteins via Comparison with Accurate Quantum Chemical Calculations on Peptides. J Phys Chem B. 2001; 105:6474–6487.
51. Jorgensen WL, Chandrasekhar J, Madura JD, Impey RW, Klein ML. Comparison of Simple Potential Functions for Simulating Liquid Water. J Chem Phys. 1983; 79:926.
52. Hess B, Bekker H, Berendsen HJC, Fraaije JGEM. LINCS: A Linear Constraint Solver for Molecular Simulations. J Comput Chem. 1997; 18:1463–1472.
53. Miyamoto S, Kollman PA. Settle: An Analytical Version of the SHAKE and RATTLE Algorithm for Rigid Water Models. J Comput Chem. 1992; 13:952–962.
54. Essmann U, Perera L, Berkowitz ML, Darden T, Lee H, Pedersen LG. A Smooth Particle Mesh Ewald Method. J Chem Phys. 1995; 103:8577–8593.
55. Verlet L. Computer “Experiments” on Classical Fluids. I. Thermodynamical Properties of Lennard-Jones Molecules. Phys Rev. 1967; 159:98.
56. Hukushima K, Nemoto K. Exchange Monte Carlo Method and Application to Spin Glass Simulations. J Phys Soc Jpn. 1996; 65:1604–1608.
57. Sugita Y, Okamoto Y. Replica-exchange Molecular Dynamics Method for Protein Folding. Chem Phys Lett. 1999; 314:141–151.
58. Patriksson A, van der Spoel D. A Temperature Predictor for Parallel Tempering Simulations. Phys Chem Chem Phys. 2008; 10:2073–2077. [PubMed: 18688361]
59. Nosé S. A Molecular Dynamics Method for Simulations in the Canonical Ensemble. Mol Phys. 1984; 52:255–268.
60. Hoover WG. Canonical Dynamics: Equilibrium Phase-space Distributions. Phys Rev A. 1985; 31:1695. [PubMed: 9895674]
61. Daura X, Gademann K, Jaun B, Seebach D, van Gunsteren WF, Mark AE. Peptide Folding: When Simulation Meets Experiment. Angew Chem Int Ed. 1999; 38:236–240.
62. Bleiholder C, Dupuis NF, Wyttenbach T, Bowers MT. Ion Mobility-Mass Spectrometry Reveals a Conformational Conversion from Random Assembly to β-Sheet in Amyloid Fibril Formation. Nat Chem. 2011; 3:172–177. [PubMed: 21258392]
63. Do TD, LaPointe NE, Economou NJ, Buratto SK, Feinstein SC, Shea J-E, Bowers MT. Effects of pH and Charge State on Peptide Assembly: The YVIFL Model System. J Phys Chem B. 2013; 117:10759–10768. [PubMed: 23937333]
64. Naruto K, Minoura K, Okuda R, Taniguchi T, In Y, Ishida T, Tomoo K. Interplay Between I308 and Y310 Residues in the Third Repeat of Microtubule-Binding Domain is Essential for Tau Filament Formation. FEBS Lett. 2010; 584:4233–4236. [PubMed: 20837015]
65. Zhong Q, Congdon EE, Nagaraja HN, Kuret J. Tau Isoform Composition Influences Rate Extent of Filament Formation. J Biol Chem. 2012; 287:20711–20719. [PubMed: 22539343]

66. Yu X, Luo Y, Dinkel P, Zheng J, Wei G, Margittai M, Nussinov R, Ma B. Cross-seeding and conformational Selection between Three- Four-repeat Human Tau Proteins. J Biol Chem. 2012; 287:14950–14959. [PubMed: 22393063]

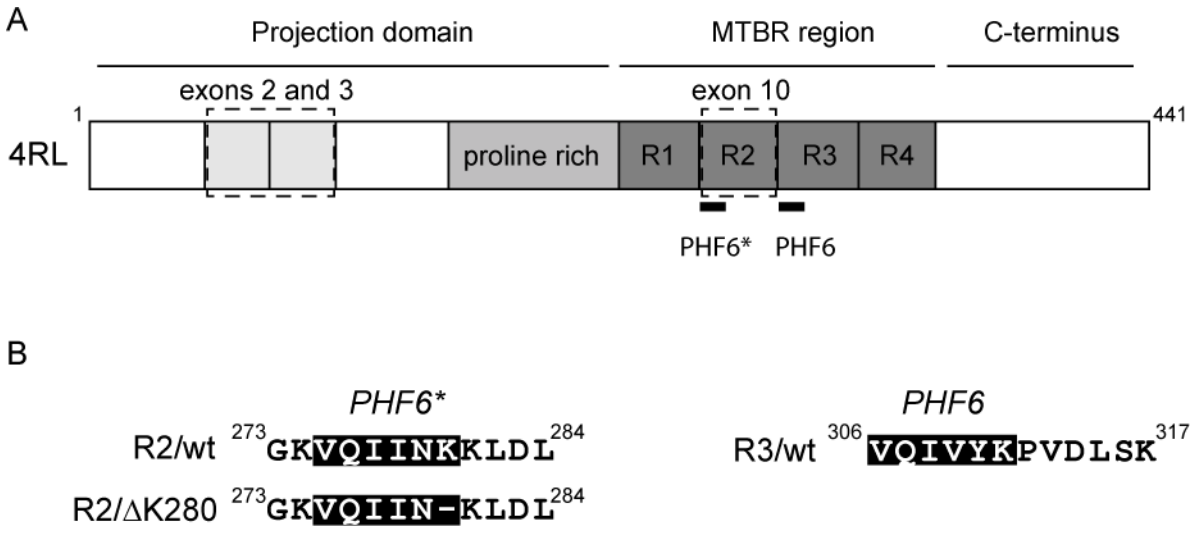

Figure 1.

(A) Schematic diagram of the longest Tau isoform found in the human CNS (4-repeat; 4R). Dashed boxes show the location of alternatively-spliced exons 2, 3, and 10. The microtubule binding region (MTBR) contains four imperfect repeats units (R1–R4) along with the PHF6 and PHF6* sequences (locations marked). The amino terminal projection domain contains a proline-rich region and two alternatively-spliced exons. (B) Amino acid sequences of the R2/wt, R2/ΔK280 and R3/wt peptides in the current study, with the locations of PHF6 and PHF6* indicated. This figure is adapted in part from Ref 35. Copyright 2013 Royal Society of Chemistry.

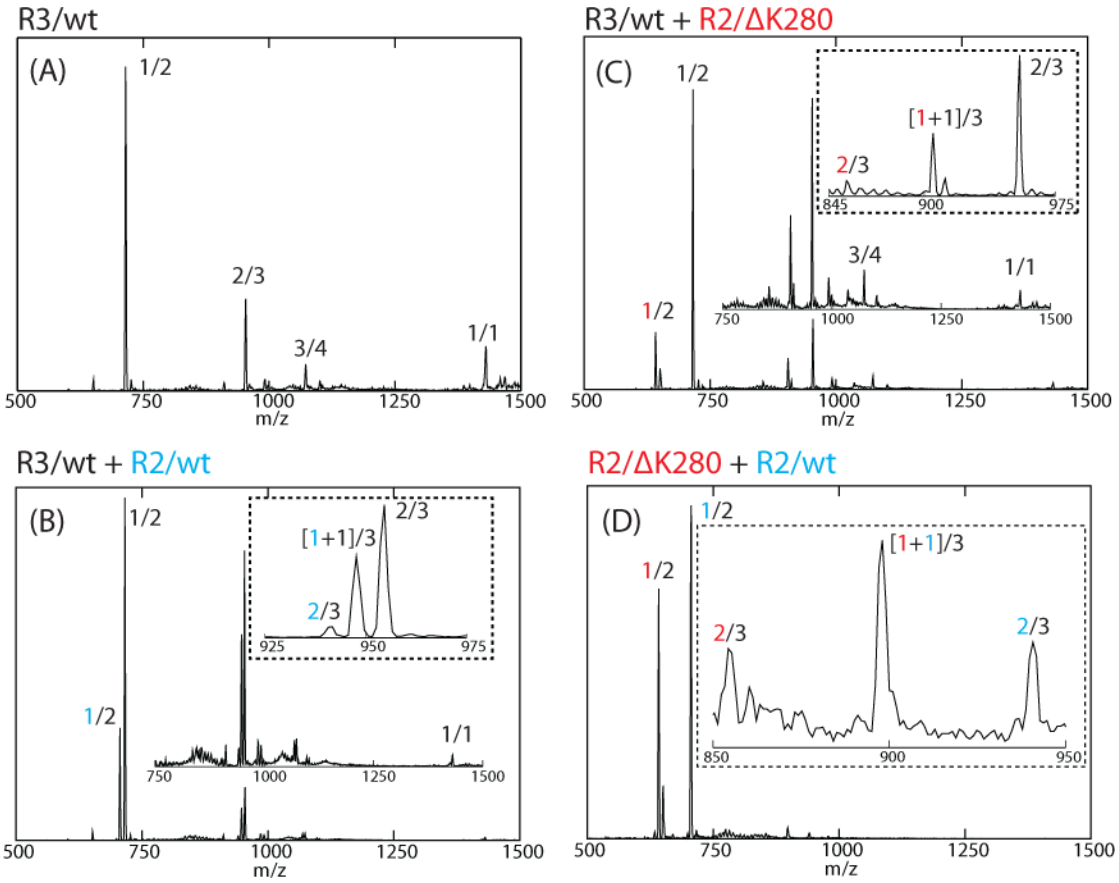

Figure 2.

nano-ESI mass spectra of (A) R3/wt and the binary mixtures of (B) R3/wt and R2/wt, (C) R3/wt and R2/ΔK280, and (D) R2/wt and R2/ΔK280 at 50 μM total peptide concentration. The peaks are annotated with *n/z* where *n* is the oligomer size and *z* is the charge. *n* is labeled in black, blue and red for the species corresponding to R3/wt, R2/wt, and R2/ΔK280 respectively. The insets in panels B–D show the relative abundance of heterodimers vs. homodimers in each binary mixture.

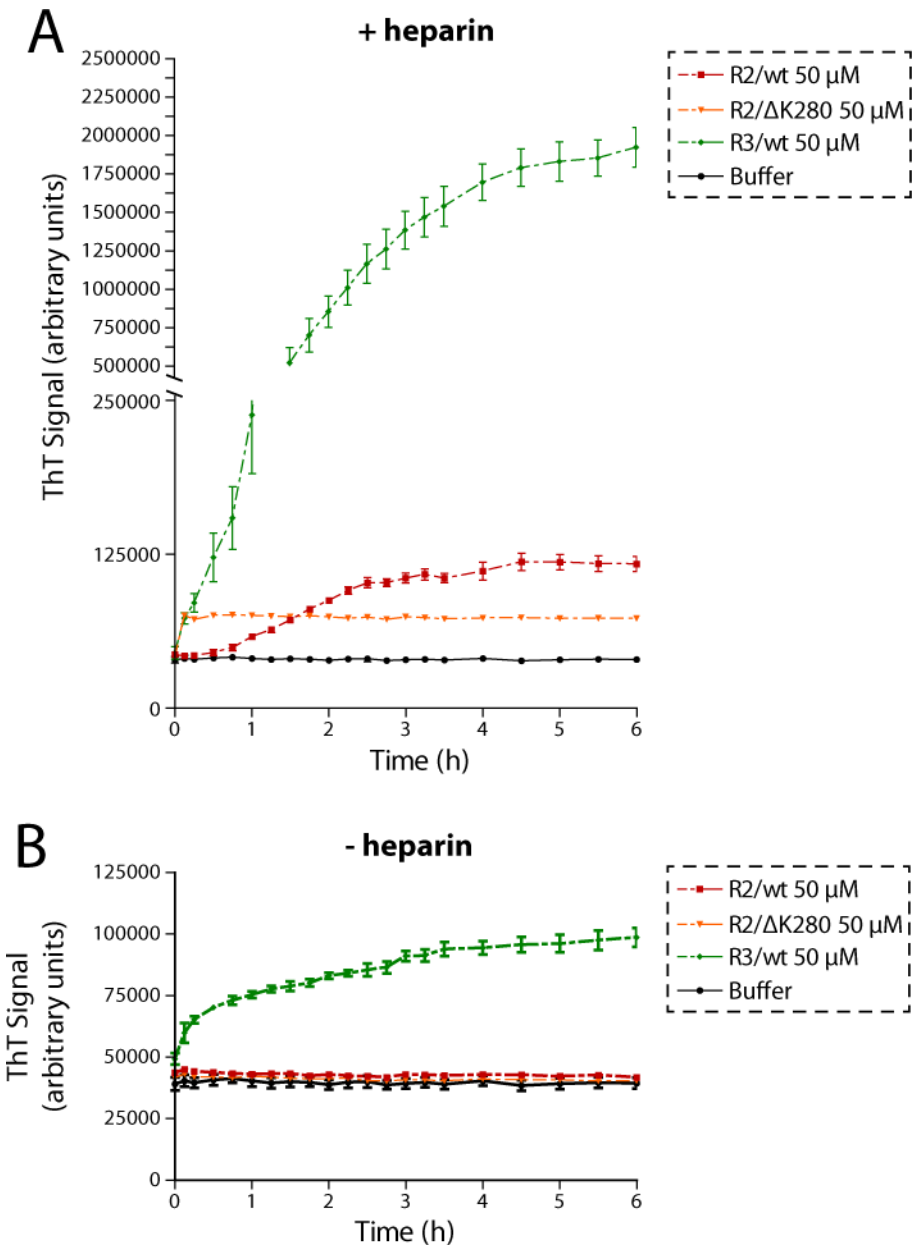

Figure 3.

Thioflavin T assays reveal differences in the extent and kinetics of aggregation between the individual peptides. R2/wt, R2/ΔK280, and R3/wt peptides were incubated separately at 50 μM in buffer containing ThT, with (A) or without (B) heparin over the first 6 h. Data shown are the average of three independent trials ±SEM.

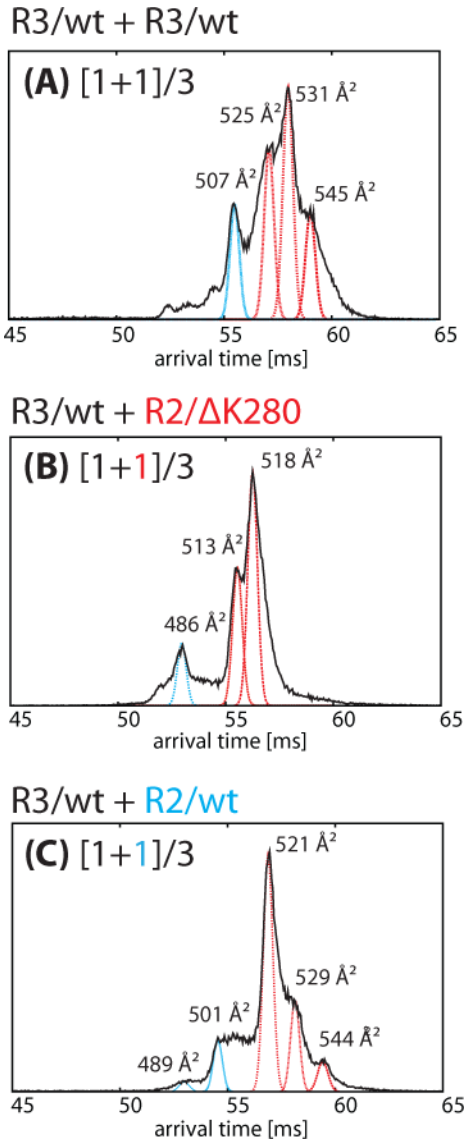

Figure 4.

Representative ATDs of (A) R3/wt homodimer peak, and of heterodimers of (B) R3/wt + R2/ΔK280 and (C) R3/wt + R2/wt. Each feature is annotated with an experimental cross section σ_{exp} obtained from IM-MS experiments.

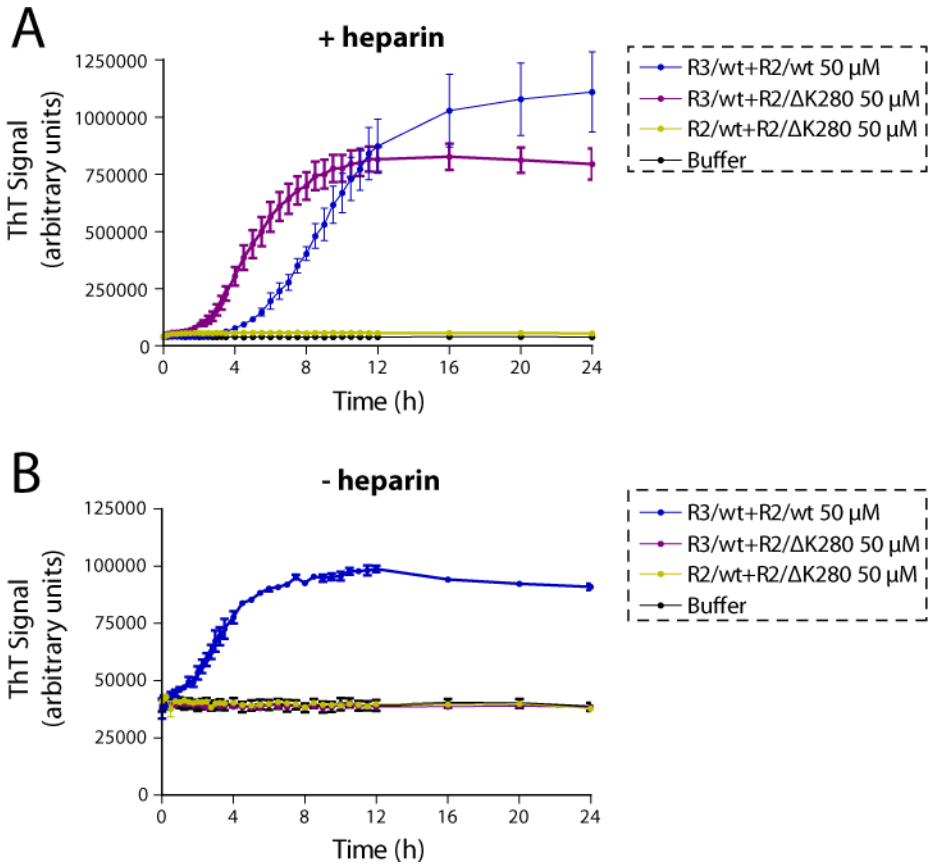

Figure 5.

Thioflavin T assays reveal differences in the extent and kinetics of aggregation of the binary mixtures of R2/wt, R2/ΔK280, and R3/wt peptides incubated at 50 μM total in buffer containing ThT, with or without heparin. (A) Aggregation over 24h in the presence of heparin. (B) Aggregation over 24 h in the absence of heparin. Data shown are the average of three independent trials ±SEM.

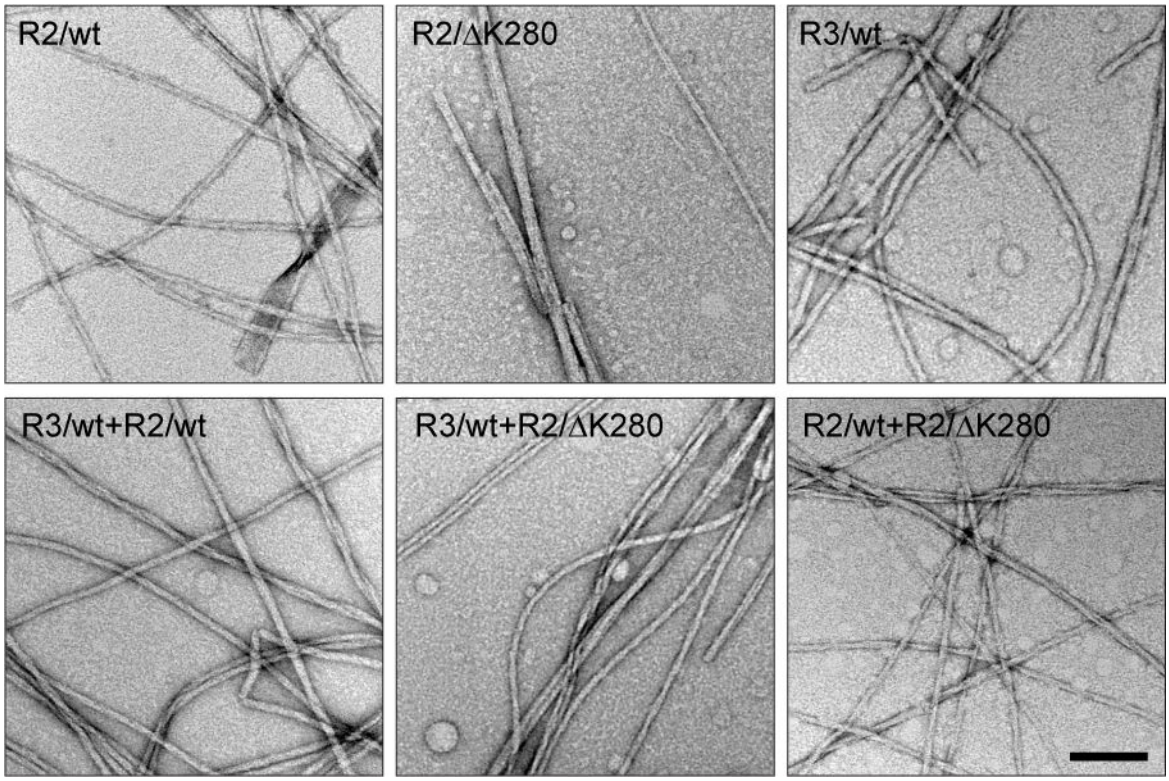

Figure 6.

Transmission electron microscopy of R2/wt, R2/ΔK280, and R3/wt peptides and their various binary mixtures. Peptides (50 μM total) were aggregated for 24h in the presence of heparin (12.5 μM). All individual peptides and their binary mixtures form fibrillar aggregates. Scale bar = 100 nm.

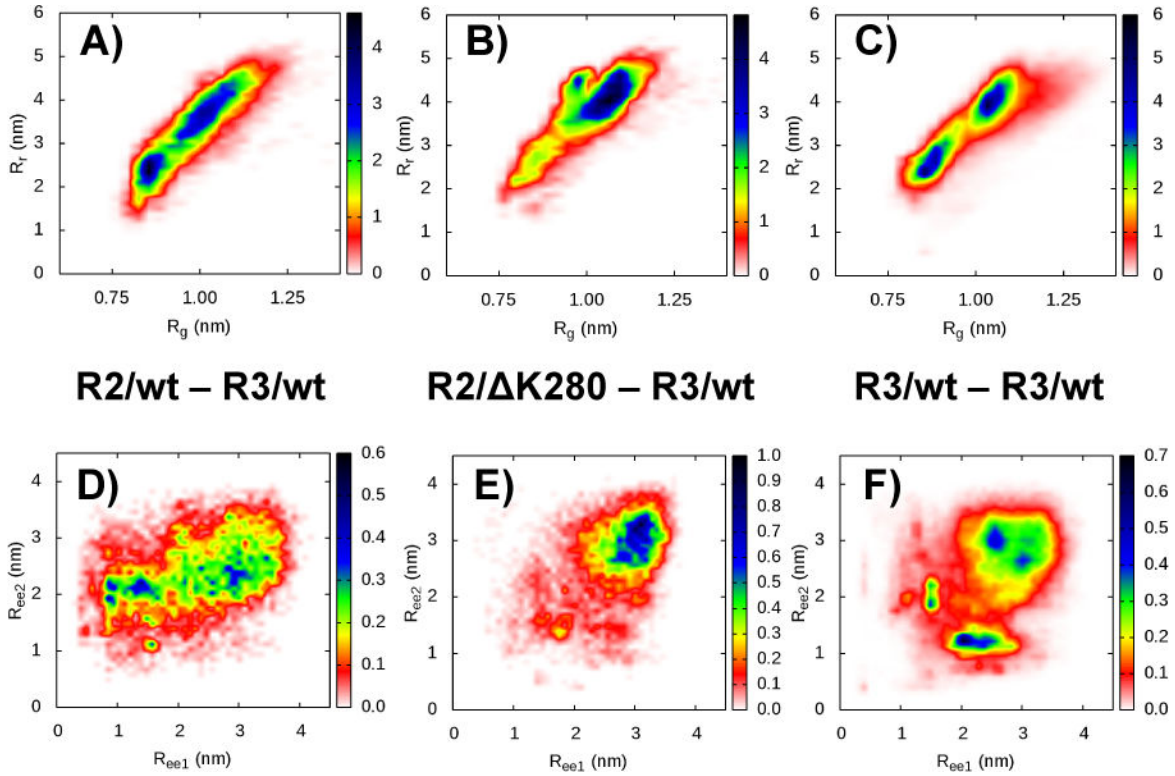

Figure 7.

Conformations sampled by the peptide dimers for R2/wt–R3/wt (A) and (D), R2/ΔK280–R3/wt (B) and (E), and R3/wt–R3/wt (C) and (F). The potential mean force (PMF) is generated from the distributions of the end-to-end distances (R_{ee}) of the individual monomers composing the dimers (d, e, and f) and the distributions of the radius of gyration of the dimers with the reduced end-to-end distances ($R_r = \sqrt{R_{ee1}^2 + R_{ee2}^2}$) of the dimers (A, B, and C). R2/wt–R3/wt and R3/wt–R3/wt dimers sample both extended and compact conformations; R2/ΔK280–R3/wt dimers predominantly prefer extended structures.

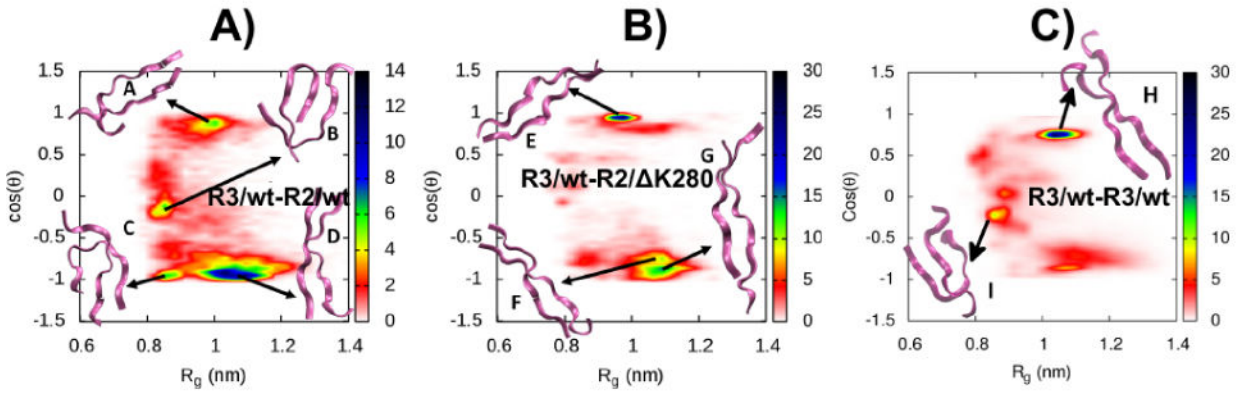

Figure 8.

Relative orientations of the monomers composing the dimers for (A) R2/wt–R3/wt, (B) R2/ΔK280–R3/wt, and (C) R3/wt–R3/wt. Parallel alignment: $\cos\theta + 1$; antiparallel: $\cos\theta \approx -1$. Both the heterodimer (R2–R3) aggregates sample parallel≈ and antiparallel conformations, with antiparallel conformations being relatively preferred. R2/ΔK280 more ordered than R2/wt. R3–R3 homodimers are the most ordered dimers and prefer parallel conformations. Representative structures corresponding to significant populations are shown.

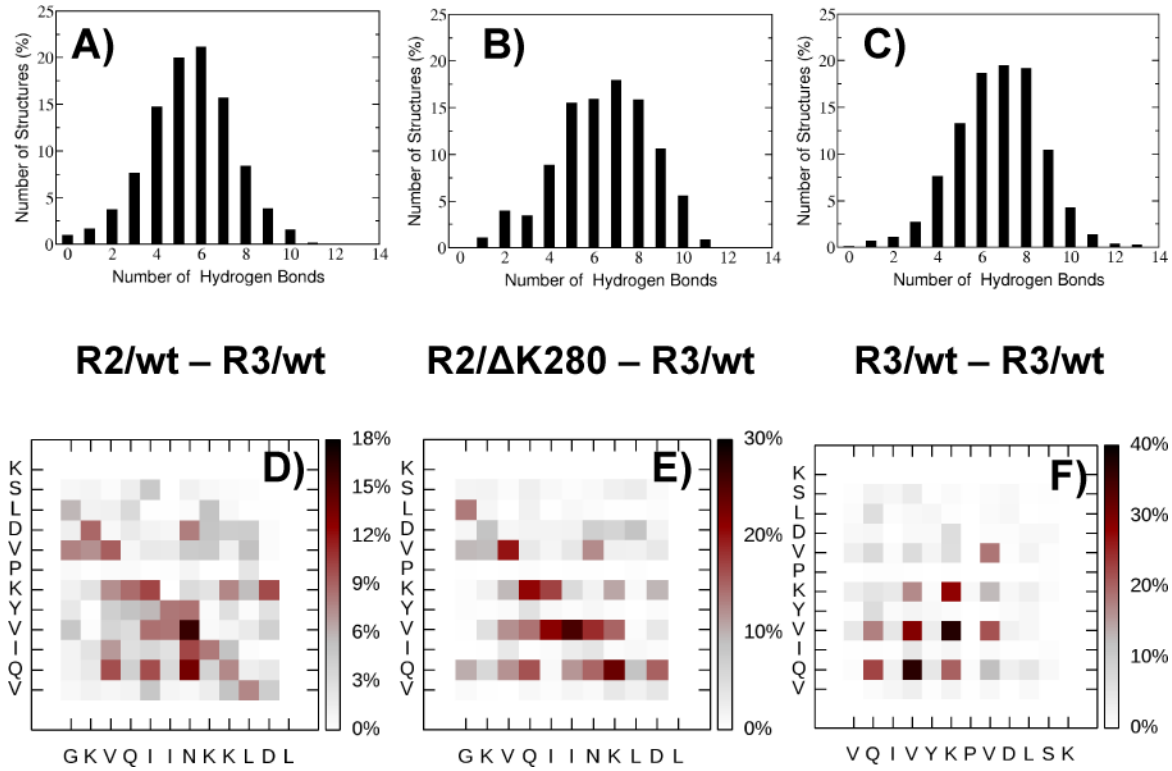

Figure 9.

The distributions of the number of hydrogen bonds between the peptide monomers for (A) R2/wt–R3/wt, (B) R2/ΔK280–R3/wt and (C) R3/wt–R3/wt. All the dimers show multiple stable hydrogen bond formations. The distributions of the hydrogen bonds between individual amino acid residues of the monomers with respect to the simulation time are shown in (D), (E), and (F) for R2/wt–R3/wt, R2/ΔK280–R3/wt and R3/wt–R3/wt dimers, respectively. PHF6 (VQIVYK in R3/wt) and PHF6* (VQIINK in R2/wt and R2/ΔK280) contribute to the majority of the hydrogen bonds (49% in R2/wt–R3/wt, 57% in R2/ΔK280–R3/wt, and 59% in R3/wt homodimers).